Redox Biology 32 (2020) 101452

Contents lists available at ScienceDirect

Redox Biology

journal homepage: www.elsevier.com/locate/redox

Ginsenoside Rh2 pretreatment and withdrawal reactivated the pentose phosphate pathway to ameliorate intracellular redox disturbance and promoted intratumoral penetration of adriamycin

Jiali Liu[a,1], Qingyun Cai[a,1], Wenjie Wang[a,1], Meng Lu[b], Jianming Liu[c], Fang Zhou[a], Minjie Sun[d], Guangji Wang[a,**], Jingwei Zhang[a,*]

[a] Key Laboratory of Drug Metabolism and Pharmacokinetics, State Key Laboratory of Natural Medicines, China Pharmaceutical University, Nanjing, Jiangsu, China
[b] Nanjing Drum Tower Hospital, The Affiliated Hospital of Nanjing University Medical School, Nanjing, Jiangsu, China
[c] Clinical Pharmacology Institute, Nanchang University, Nanchang, China
[d] Department of Pharmaceutics, China Pharmaceutical University, Nanjing, Jiangsu, China

ARTICLE INFO

Keywords:
Pentose phosphate pathway reactivation
Intracellular redox status
Intratumoral penetration
Mathematical modeling
"Ginsenoside Rh2-adriamycin" sequential treatment

ABSTRACT

Improving the limited penetration, accumulation and therapeutic effects of antitumor drugs in the avascular region of the tumor mass is crucial during chemotherapy. P-gp inhibitors have achieved little success despite significant efforts. Excessive P-gp inhibition disturbed the kinetic balance between intracellular accumulation and intercellular penetration, thus resulting in a more inhomogeneous distribution of substrate drugs. Here, we found that ginsenoside Rh2 pretreatment mildly downregulated P-gp expression through reactivating the pentose phosphate pathway and rebalancing redox status. This mild P-gp inhibition not only significantly increased the growth inhibition effect and accumulation profile of adriamycin (ADR) throughout the multicellular tumor spheroid (MCTS) but also had unique advantages in improving drug penetration. Furthermore, we developed a novel individual-cell-based PK-PD integrated model and proved that metabolic reprogramming and redox rebalancing-based P-gp regulation was sufficient to increase the ADR effect in both central and peripheral cells of MCTS. Thus, a "ginsenoside Rh2-ADR" sequential regimen was proposed and exhibited a potent antitumor effect in vivo. This novel P-gp inhibition via metabolic reprogramming and redox rebalancing provided a new idea for achieving better antitumor effects in the tumor avascular region during chemotherapy.

1. Introduction

Cancer represents a major disease burden globally. Chemotherapy is one of the most commonly used treatments in oncology and depends heavily on the efficient penetration of antitumor drugs into the tumor mass and reaching all tumor cells with sufficient concentration [1]. However, limited intratumoral distribution and intracellular accumulation in the central region of the tumor mass are common and result in treatment resistance [2,3].

Interfering with cell membrane efflux proteins was among the very early attempts to increase the intracellular drug concentration [4]. However, this field has achieved little success despite significant efforts [3,5,6]. P-glycoprotein (P-gp), a well-known highly expressed efflux protein in the tumor mass, has been identified as a double-edged sword in the intratumoral pharmacokinetics of a wide range of anticancer drugs, such as adriamycin (ADR). On the one hand, drug efflux by P-gp hinders the intracellular accumulation of substrate drugs [7]; on the other hand, it promotes the transcellular penetration of substrate drugs

Abbreviations: ADR, adriamycin; Rh2, 20(S)-ginsenoside Rh2; SLCs, single-layered cells; MCTS, multicellular tumor spheroid; ROS, reactive oxygen species; G6PD, glucose-6-phosphate dehydrogenase; NADP, nicotinamide adenine dinucleotide phosphate; NADPH, reduced nicotinamide adenine dinucleotide phosphate; G-6-P, glucose-6-phosphate; F-6-P, fructose-6-phosphate; 6-PG, 6-phosphoglycerate; R-5-P, ribose-5-phosphate; Ribu-5-P, ribulose-5-phosphate; Xylu-5-P, xylulose-5-phosphate; S-7-P, sedoheptulose-7-phosphate; E-4-P, erythrose-4-phosphate; GSH, reduced glutathione; GSSG, oxidized glutathione

* Corresponding author. Key Laboratory of Drug Metabolism and Pharmacokinetics, China Pharmaceutical University, 24 Tong Jia Xiang, Nanjing, Jiangsu, 210009, China.
** Corresponding author. Key Laboratory of Drug Metabolism and Pharmacokinetics, China Pharmaceutical University, 24 Tong Jia Xiang, Nanjing, Jiangsu, 210009, China.
E-mail addresses: guangjiwang@hotmail.com (G. Wang), zhangjw_cnnj@sina.com (J. Zhang).
[1] J.L. Liu, Q.Y. Cai and W.J. Wang contributed equally to this work.

https://doi.org/10.1016/j.redox.2020.101452
Received 5 September 2019; Received in revised form 19 January 2020; Accepted 3 February 2020
Available online 05 February 2020

[3,8]. Thus, the kinetic balance during P-gp blockade is crucial. Only if the diffusion rate of the substrate drug remains greater than the cell internalization rate in all cell layers can the intracellular retention in center cells be uninfluenced by changes in intercellular motion, enabling deeper avascular penetration [9]. Current developments in P-gp inhibitors were accomplished using the concept of better P-gp binding affinity and focused mainly on increasing drug accumulation within the whole tumor mass but neglected the effect on the intratumoral spatial pharmacokinetics [10]. Excessive P-gp inhibition results in a reciprocal decrease in the available drug molecules for deeper penetration along with significantly increased intracellular accumulation in cells near vessels[[8,11]]. Consequently, the drug supply outside the central cells becomes insufficient, and the drug distribution becomes more inhomogeneous [9]. In comparison with the existing strong P-gp blockade, mild P-gp interference with consideration for the kinetic balance would be more efficient.

Downregulating P-gp expression to a normal status through reprogramming the abnormal upstream pathway within the tumor mass is a preferable strategy for mild P-gp interference. Distinctive cell metabolomic profile and abnormal endogenous oxidative stress status are two main tumor characteristics. Previously, we found a cascade effect of metabolic reprogramming and redox imbalance on P-gp expression within the tumor mass. The pentose phosphate pathway (PPP) was spontaneously impaired along with tumor growth. The impaired PPP disturbed redox cycling and thereby caused Chk2/p53/p65 pathway-mediated P-gp induction [12]. Thus, here, we tried to find novel strategies for P-gp inhibition based on metabolic reprogramming. We found that Rh2 pretreatment and withdrawal (to interfere with P-gp expression based on metabolic reprogramming) exhibited superior effects on optimizing intratumor penetration and on the antitumor effect of ADR, with both in vitro and in vivo evidence. This superior effect was further explained with a novel individual-cell-based PK-PD integrated model.

2. Materials and methods

2.1. Materials

Adriamycin (ADR) was purchased from Chemlin Chemical Industry (Jiangsu, China). 20(S)-ginsenoside Rh2 (Rh2, purity > 98%) was purchased from Jilin University (Changchun, China). HPLC-grade acetonitrile and methanol were purchased from Merck (Germany). Deionized water was prepared by a Milli-Q system (Millipore, USA). Reactive oxygen species (ROS) assay kits, lipid peroxidation MDA assay kits (MDA) and glutathione (GSH)/oxidized glutathione (GSSG) test kits were purchased from Beyotime Institute of Biotechnology (Jiangsu, China). Protein carbonylation assay (PCA) kits and $NADP^+$/NADPH quantitation colorimetric kits were purchased from BioVision, Inc. (USA). A glucose-6-phosphate dehydrogenase (G6PD) activity assay kit was purchased from Cell Signaling Technology (USA).

2.2. MCF-7 cell culture and spheroid cell culture

MCF-7 human breast carcinoma cells were purchased from the American Type Culture Collection. The cells (passages 10 to 20) were cultured in RPMI 1640 medium supplemented with 10% fetal bovine serum and 100 U ml^{-1} penicillin and streptomycin (Invitrogen, Carlsbad, CA) at 37 °C with 5% CO_2, and the medium was changed every other day. The culture of MCF-7 MCTS was performed as we described previously [12]. The uniform and compact MCTS were selected under an automated digital microscope (Lionheart FX, Biotek, Vermont, USA).

2.3. Knockdown of G6pd

G6pd knockdown in MCF-7 MCTS was performed with Stealth Select RNAiTM siRNA, which was designed and synthesized by Invitrogen (Life Technologies, USA) to selectively target human G6pd mRNA. The sequence of G6pd siRNA was 5′-ACG AGC UGA UGA AGA GAG UGG GUU U-3'. RNAi duplex-Lipofectamine® RNAiMAX (Life Technologies, USA) complexes were prepared and then mixed with the appropriate number of MCF-7 cells when plating. Control siRNA, a nontargeting siRNA, was used as a negative control.

2.4. Cell viability assay

MCTS was exposed to a series of concentrations of ADR for 72 h at 37 °C with 5% CO_2. After treatments, cell viabilities were measured by a CCK-8 Assay Kit (KeyGEN BioTech, Nanjing, China) and quantified relative to those in wells without drugs. IC_{50} values were calculated from inhibition curves using GraphPad Prism 6.

2.5. Cellular retention assay

At different intervals after drug administration, single-layered cells (SLCs) and MCTS were rinsed with cold PBS and lysed by three freeze-thaw cycles. Protein concentrations were measured by the Bradford method, and ADR concentration was determined by LC-MS/MS [13]. All experiments were conducted in triplicate.

2.6. Drug penetration assay

The penetration of ADR into the MCTS or tumor mass was analyzed under a laser scanning confocal microscope (LSM 800, Carl Zeiss, Oberkochen, Germany).

At different intervals after drug administration, MCTS were collected, and drug fluorescence was detected. Z-stack images were obtained by scanning a spheroid every 10 μm from the top of the spheroid with a total scan range of 200 μm in depth. A plane approximately halfway through the z-stack image was chosen for quantification, and the fluorescence intensities were plotted against the radius.

The collected tumors were immediately embedded in OCT compound, frozen and stored at −80 °C. Next, 10-μm-thick cryosections were cut at approximately 100 μm intervals for each tumor and mounted on glass slides. Fluorescence was imaged using a laser scanning confocal microscope (LSM 800, Carl Zeiss, Oberkochen, Germany), and the fluorescence intensities of ADR in the tumor cryostat sections were plotted against the intersecting line.

2.7. GC-MS and LC-Q/TOF-MS-based metabolomics assays

The samples of tumor tissues and MCF-7 MCTS with or without Rh2 treatments were processed as we described previously [12]. Then, they were subjected to GC-MS or LC-Q/TOF-MS for metabolomics assays with metabolite identification and multivariate data analysis. The compounds involved in the PPP were semiquantified through the peak area of each compound weighted by the internal standard and protein concentration.

2.8. Intracellular PCA, MDA, ROS, GSSG/GSH, and $NADP^+$/NADPH assays

The MCF-7 MCTS with/without G6pd knockdown were treated with Rh2 (10 μM) for 3 days. The intracellular protein carbonylation, lipid peroxidation, ROS, GSH/GSSG, $NADP^+$/NADPH levels were assayed according to the instructions for each assay.

Intracellular protein carbonylation was detected using a Protein Carbonyl Content Assay Kit. After incubating the MCTS lysate with diluted fluorophore (fluoroscein-5-thiosemicarbazide) overnight, the protein carbonyl content was determined by the generation of a stable fluorometric signal (Ex/Em 485/535 nm), and adjusted to the protein concentration determined by the BCA assay.

Intracellular protein lipid peroxidation was measured with a Lipid

Peroxidation MDA Assay Kit. Briefly, MCTS were lysed, incubated with mixed assay buffer, heated at 100 ˚C for 15 min, cooled to room temperature and centrifuged at 1,000 × *g* for 10 min. The supernatant was collected, and its absorbance was detected at 532 nm.

Intracellular ROS levels were assessed with a reactive oxygen probe (DCFH-DA, 10 μM). After incubation with DCFH-DA in the dark at 37 ˚C for 2 h, the MCTS were washed and lysed with NaOH:methanol (v:v = 1:1) solution. The cell lysate was centrifuged, and the supernatant was collected for determination at 535 nm (with 488 nm excitation).

Intracellular GSSG and GSH levels were measured by using the GSH/GSSG Test Kit. In brief, MCTS were lysed, and each sample was divided into two parts. In one part, the intracellular GSSG was catalyzed to GSH, and total GSH was detected with 5,5-dithio-bis(2-nitrobenzoic) acid (DTNB). In the other part, intracellular GSH was pre-excluded before GSSG catalysis, allowing the detection of intracellular GSSG. The concentration of intracellular GSH was obtained by subtracting the GSSG from the total GSH.

Intracellular $NADP^+$ and NADPH levels were determined with an $NADP^+$/NADPH Quantitation Colorimetric Kit. Briefly, MCTS were lysed, and each sample was divided into two parts. In one part, intracellular $NADP^+$ was catalyzed to NADPH, and total NADPH was detected. In the other part, the intracellular $NADP^+$ was pre-decomposed with a water bath, and then intracellular NADPH was detected. The concentration of intracellular $NADP^+$ was calculated by subtracting the NADPH from the total NADPH.

2.9. G6PD activity assay

The enzyme activity of G6PD was assayed by a G6PD Activity Assay Kit. MCF-7 MCTS or tumor tissues were lysed with ice-cold cell lysis buffer plus PMSF. After centrifugation, the supernatant was collected and mixed with detection solution. The fluorescence intensity was read with excitation at 540 nm and emission at 590 nm to obtain the kinetic curves.

2.10. Western blot

Tumor or cell samples were lysed on ice with a handheld homogenizer in lysis buffer supplemented with 100 μM PMSF and 0.1% (v/v) protease inhibitor cocktail (Beyotime Biotechnology, China). Whole-cell protein was extracted by centrifugation (12,000 × *g*, 10 min, 4 ˚C). Nuclear protein was prepared with a KeyGen Mitochondria/Nuclei Isolation Kit (KeyGEN BioTECH, China). After separation on a 10% SDS-polyacrylamide gel, the proteins were transferred onto a polyvinylidene difluoride membrane (Bio-Rad, Hercules, CA, USA), which was then blocked with 5% nonfat milk and further incubated with the primary antibodies overnight at 4 ˚C. The following antibodies were used to detect protein expression: anti-G6PD (1:1000, Abcam, Cat#AB993), anti-Chk2 (1:1000, Abcam, Cat#AB47433), anti-p53 (1:1000, Abcam, Cat#AB26), and anti-p65 (1:1000, Biogot Technology, Cat#BS1254). Before detection, horseradish peroxidase-conjugated secondary antibody (goat anti-rabbit 1:10000, Cell Signaling Technology, Cat#7074S or horse anti-mouse 1:10000, Cell Signaling Technology, Cat#7076S) was added and incubated for 1 h at 37 ˚C, and the signals could be detected using an Enhanced Chemiluminescence Kit (Thermo Fisher Scientific, Waltham, MA, USA) and captured using a ChemiDoc XRS +System (Bio-Rad, Hercules, CA, USA). Signal intensities were normalized to GAPDH (for proteins from whole cells, Biogot Technology, Cat#MB9293) or histone (for nuclear proteins, Cell Signaling Technology, Cat#4499S).

2.11. Quantitative real-time PCR assay

MCF-7 MCTS were suspended in a High Pure RNA Isolation Kit (RNAiso Plus, Takara Bio, Japan), and the total RNA was extracted. Then, the RNA was reverse transcribed into cDNA with a PrimeScript RT Reagent Kit (Takara Bio, Japan). Quantitative real-time PCR (qPCR) was performed in a CFX96 real-time RT-PCR detection system (Bio-Rad, USA). The primers used in this study were synthesized by Invitrogen (Life Technologies, USA):

G6pd: forward primer: GGCAACAGATACAAGAACATGAA;
reverse primer: CCCTCATACTGGAAACCCACT;
β-actin: forward primer: GCGTGACATTAAGGAGAAG;
reverse primer: GAAGGAAGGCTGGAAGAG.

The qPCR conditions included a 95 ˚C initial denaturation for 90 s, followed by 40 cycles of denaturation (30 s at 95 ˚C), annealing (30 s at 60 ˚C) and extension (30 s at 72 ˚C). A melting curve was used to monitor the specificity of the primer. The relative expression of G6pd was normalized to the expression of the reference gene β-actin.

2.12. P-gp expression assay

Flow cytometry was used to determine the protein expression of P-gp as we described previously [8]. In brief, drug- or siG6pd-treated or untreated MCF-7 MCTS were fixed with 4% polyformaldehyde solution. After washing and blocking, the cells were incubated with FITC-conjugated anti-P-gp polyclonal antibody (BD Biosciences, USA) at 37 ˚C for 1 h followed by another wash. Then, the samples were loaded into a flow cytometer for analysis.

2.13. PK-PD model of ADR with or without Rh2 interference based on MCTS

An integrated PK-PD model was developed here to characterize the disposition and growth inhibition effect of ADR in different cell layers and the regulation difference resulting from two Rh2 treatment strategies. First, the translation from fluorescence intensity to intracellular drug concentration was processed using the mass balance law. The PK model for ADR disposition was established based on the model we described previously with several modifications [9]. Briefly, each MCTS was considered as regular spheroids containing a series of cell layers separated by small intercellular spaces. The intracellular accumulation profile of ADR in each cell layer was modeled using compartment models with three parameters, X_{mn}/D, K_n and P_n. The intercellular penetration was described by ordinary differential equations with the parameter K_{pn}. Four factors, α, β, ω, and γ, were added to represent the regulatory effects of different Rh2 treatment strategies on the ADR kinetic profile. For the pharmacodynamic part, different types of PD models were tested to describe the relationship between intracellular drug accumulation and the therapeutic effect. Considering the working mechanism of ADR and our previous PD model for SLCs [14], a logistic model was finally chosen to describe the sigmoidal PD profile. The final integrated PK-PD model was constructed as follows:

Fluorescence intensity-intracellular concentration translation:

$$C_n = \frac{F_n}{F_{n-1}} * C_1;\ V_{cell} = \frac{4}{3} * \pi * \left(\frac{D_{cell}}{2}\right)^3;\ N_n = \frac{\frac{4}{3} * \pi * \left(\frac{D_{cell} * (2n-1)}{2}\right)^3 - \frac{4}{3} * \pi * \left(\frac{D_{cell} * (2n-3)}{2}\right)^3}{V_{cell}};\ M_{spheroid} = \sum_1^m C_n * V_{cell} * N_n;\ (\text{n= 1, 2, ...m})$$

PK part:

Intracellular accumulation profile at cell layer n:

$$g_n(t) = \frac{dC_n}{dt} = \beta_n * K_n * \triangle C_n * \left(1 - \frac{C_n}{\alpha_n * X_{mn}}\right);\ \triangle C_n = \gamma_n * P_n * D_n - C_n;$$

Intercellular penetration profile at cell layer n:

$$\frac{dD_n}{dt} = \omega_n * K_{pn} * (D_{n+1} - D_n);$$

When ADR was administered without Rh2 treatment, the values of α_n, β_n, γ_n and ω_n were identified as constant 1, (n = 1, 2, …m).

PD part:

$$R = R_{min} + \frac{R_{max} - R_{min}}{1 + 10^{?Log\psi - Log\phi)*r}};\ C_n = \frac{\sum_1^m (\eta_n * N_n)}{\sum_1^m N_n};\ \eta_n = \int_0^T \left(\int g_n(t) * dt \right) * dt;\ (n = 1, 2, \ldots m)$$

where n is the number of cell layers from the center to the periphery; F_n is the average fluorescence intensity at the n_{th} cell layer; D_{cell} is the diameter of a single cell; V_{cell} is the volume of a single cell; m is the total cell number; N_n is the number of cells in the n_{th} cell layer; and $M_{spheroid}$ represents the number of moles of drugs in the whole MCTS. C_n is the intracellular drug concentration in the n_{th} cell layer; D_n represents the drug concentration outside the n_{th} cell layer; X_{mn}, K_n and P_n describe the intracellular drug concentration threshold, the transport rate constant and the permeability coefficients in the n_{th} cell layer, respectively; K_{pn} describes the drug penetration rate within the intercellular space of the n_{th} cell layer; and four regulatory factors, α, β, ω, and γ, represent the regulatory effect of Rh2 treatment on X_{mn}, K_n, P_n and K_{pn}, respectively. R describes the average growth inhibition rate of ADR on MCTS; $R_{max}$and R_{min} represent the maximum and minimum stable levels of ADR growth inhibition effect on MCTS, respectively; ψ describes the sensitivity of MCTS to ADR inhibition; ϕ is the average drug accumulation amount in each cell; η_n is the area under the curve for the drug concentration at n_{th} cell layer at time point T; and r is the Hill coefficient.

2.14. Animal welfare and ethical statements

All animal care and experimental procedures were conducted according to the National Research Council's Guidelines for the Care and Use of Laboratory Animals and were approved by the SPF Animal Laboratory of China Pharmaceutical University (Animal authorization reference number: SYXK2016-0011). Every effort was made to minimize animal pain, suffering and distress and to reduce the number of animals used.

Healthy female BALB/c nude mice (18–22 g and 8–10 weeks old) were obtained from Shanghai SLAC Laboratory Animal Co., Ltd. (Shanghai, China). The mice were maintained in air-conditioned rooms under controlled light (12 h light: 12 h dark) and temperature (23 ± 2 °C, 55 ± 5% humidity) and fed standard laboratory food and water ad libitum. Before MCF-7 cells were transplanted into the animal, a 2-mg E_2 pellet was placed subcutaneously in the interscapular region of each mouse. Then, tumors were generated by subcutaneous injections of 5×10^6 exponentially growing MCF-7 cells into the right flank regions of the nude mice.

2.15. In vivo treatment

To examine the influence of the Rh2 pretreatment strategy on ADR penetration into the tumor mass, mice bearing MCF-7 subcutaneous tumors were divided randomly into two groups. The first group was pretreated with CMC-Na (0.01 mL g^{-1}, *i.g.*, *qd*) for 6 successive days followed by ADR administration (30 mg kg^{-1}, *i.v.*) on day 7; the second group was pretreated with Rh2 (50 mg kg^{-1}, *i.g.*, *qd*) for 6 successive days followed by ADR administration (30 mg kg^{-1}, *i.v.*) on day 7. At 30 min after ADR administration, mice were sacrificed by CO_2 asphyxiation and cervical dislocation, and tumors were collected for further experiments.

To confirm the influence of different Rh2 treatment strategies on the antitumor effect of ADR, mice bearing MCF-7 subcutaneous tumors were randomly assigned to the following six groups and administered over two cycles (7 days per cycle): (a) control group: CMC-Na (0.01 mL g^{-1}, *i.g.*, *qd*); (b) ADR group: CMC-Na (0.01 mL g^{-1}, *i.g.*, *qd*) for successive 6 days followed by ADR administration (1.5 mg kg^{-1}, *i.p.*) on day 7; the whole process was repeated twice; (c) Single-Rh2 group: CMC-Na (0.01 mL·g^{-1}, *i.g.*, *qd*) for 6 successive days followed by Rh2 administration (50 mg kg^{-1}, *i.g.*) on day 7; the whole process was repeated twice; (d) Single-Rh2 and ADR coadministration group: CMC-Na (0.01 mL·g^{-1}, *i.g.*, *qd*) for 6 successive days followed by coadministration of Rh2 (50 mg kg^{-1}, *i.g.*) and ADR (1.5 mg kg^{-1}, *i.p.*) on day 7; the whole process was repeated twice; (e) Rh2 pretreatment group: Rh2 (50 mg kg^{-1}, *i.g.*, *qd*) for 6 successive days followed by CMC-Na administration (0.01 mL·g^{-1}, *i.g.*) on day 7; the whole process was repeated twice; and (f) Rh2 pretreatment and ADR administration group: Rh2 (50 mg kg^{-1}, *i.g.*, *qd*) for 6 successive days followed by ADR administration (1.5 mg kg^{-1}, *i.p.*) on day 7; the whole process was repeated twice. Tumor volume was measured every day. On day 15, five mice in each group were sacrificed by CO_2 asphyxiation and cervical dislocation, and their tumors were collected for further experiments. Other mice in each group (n = 7) were monitored after drug withdrawal. The relationship between the tumor volume increase and drug withdrawal time was simulated by the exponential growth equation ($Y = Y_0 * \exp(k*X)$). The growth rate constant (k) and doubling time (ln (2)/k) were calculated and compared.

2.16. Immunohistochemical assay

Tumor masses were fixed in 4% paraformaldehyde overnight, embedded in paraffin and then cut into 10-μm serial sections. Tumor sections were stained with P-gp antibody and DAPI. Fluorescence was imaged with a laser scanning confocal microscope (LSM 800, Carl Zeiss, Oberkochen, Germany).

2.17. Statistical analysis

All the data are presented as the means ± S.E. of at least three independent experiments. Two-tailed Student's t-tests and one-way analysis of variance were employed for statistical analyses. Differences were considered significant at $^*p < 0.05$, $^{**}p < 0.01$, $^{***}p < 0.001$. The influence of siG6pd on Rh2 function was assessed by two-way ANOVA, and differences were considered significant at $\#p < 0.05$, $\#\#p < 0.01$, $\#\#\#p < 0.001$. Statistical data analysis was performed using GraphPad Prism 6.

3. Results

3.1. Features of ADR disposition in MCF-7 MCTS

MCF-7 cells were cultured for different numbers of days to form MCTS. According to the change profiles of diameter, area, circularity and thickness, Day 8 was chosen for further study (Fig. 1A and B) when a tightly compact spheroid was formed (Fig. 1C). The cells in the peripheral region of the MCTS were growing and possessed intact membranes, while the cells in the central region were shrunken, and their membranes were broken (Fig. 1D). The accumulation of ADR in MCTS was significantly lower than that in SLCs, and the AUC was decreased 1.92-fold (Fig. 1E). The fluorescent signal of ADR in MCTS is inhomogeneous. The closer to the MCTS core, the weaker the fluorescence intensity is (Fig. 1F). Furthermore, the IC_{50} of ADR on MCTS significantly increased with culture time, and the IC_{50} on MCTS with 8 days of culture was 38-fold higher than that on SLC (Fig. 1G).

3.2. Rh2 downregulated P-gp by reversing the suppression of PPP

As shown in Fig. 2A and Fig. 2B, when MCF-7 MCTS were treated with Rh2 for 72 h, PPP activation was accompanied by markedly

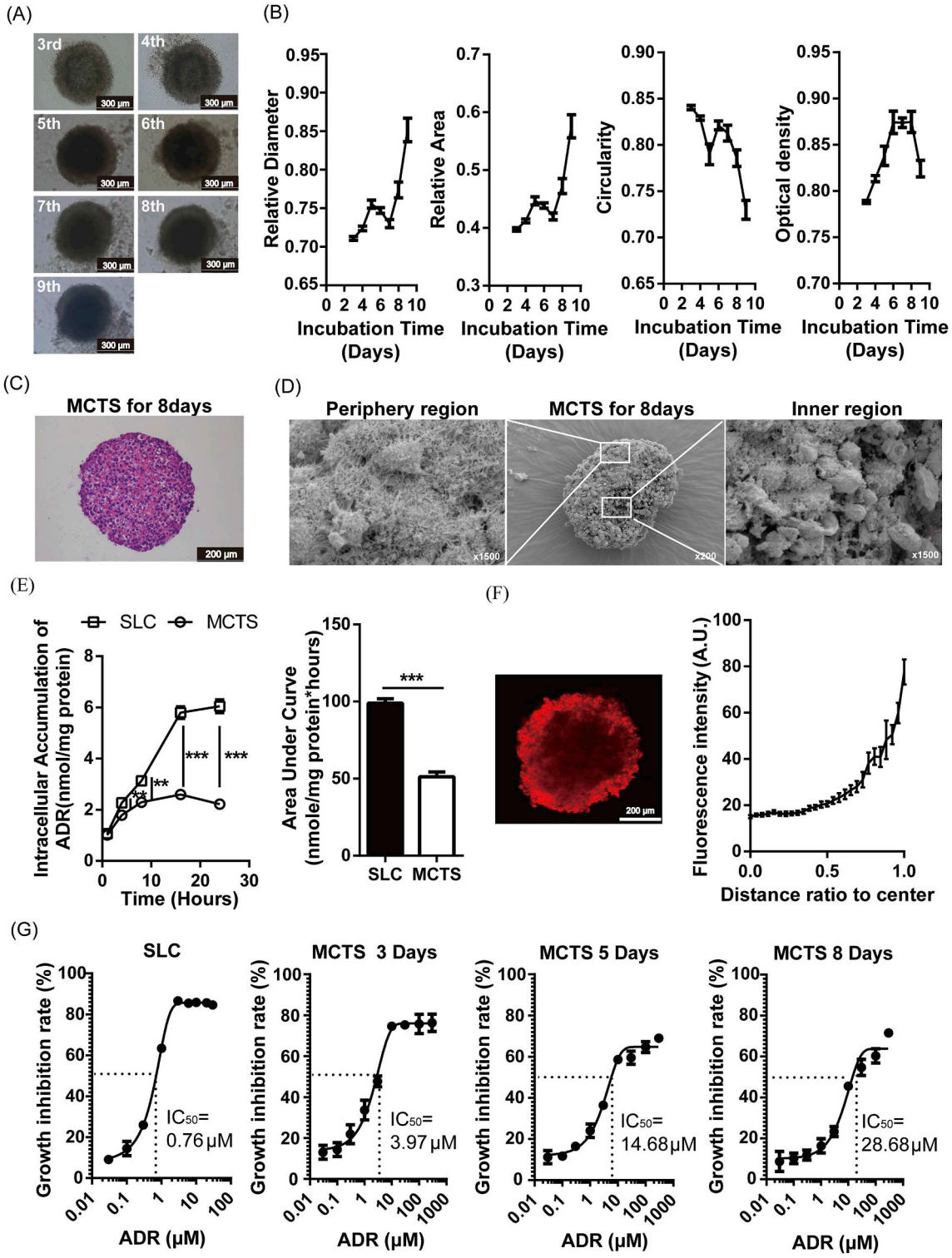

Fig. 1. Features of ADR disposition in MCF-7 MCTS. (A) MCF-7 cells were cultured for different numbers of days, and phase contrast images are shown. (B) The relative diameter, relative area, circularity and relative thickness are plotted. (C) MCF-7 MCTS after 8 days of culture were stained with H&E. (D) After the MCTS was cut along the center axis, the physiological status of cells in the inner and peripheral regions was revealed by scanning electron microscopy imaging. (E) The retention of ADR in SLC and MCTS is compared. (F) The drug penetration in MCTS is shown, and the fluorescence intensities are plotted. (G) The sensitivities of MCTS and SLC to ADR were determined. Data are presented as the mean ± S.E., **p < 0.01, ***p < 0.001.

increased protein and activity levels of G6PD. Meanwhile, increased NADPH/NADP$^+$ (Fig. 2C) and GSH/GSSG (Fig. 2D) ratios were observed after Rh2 treatment, together with decreased oxidative damage, lower protein carbonylation levels (Fig. 2E), lower lipid peroxidation levels (Fig. 2F) and decreased ROS levels (Fig. 2G). Furthermore, with Rh2 treatment, the Chk2/p53/p65 pathway was markedly suppressed (Fig. 2H). At the same time, the percentage of cells with high P-gp expression in MCF-7 MCTS decreased from 22.12% to 10.9%, and the protein level of P-gp in this cell subgroup significantly decreased to 0.65-fold of the control (Fig. 2I).

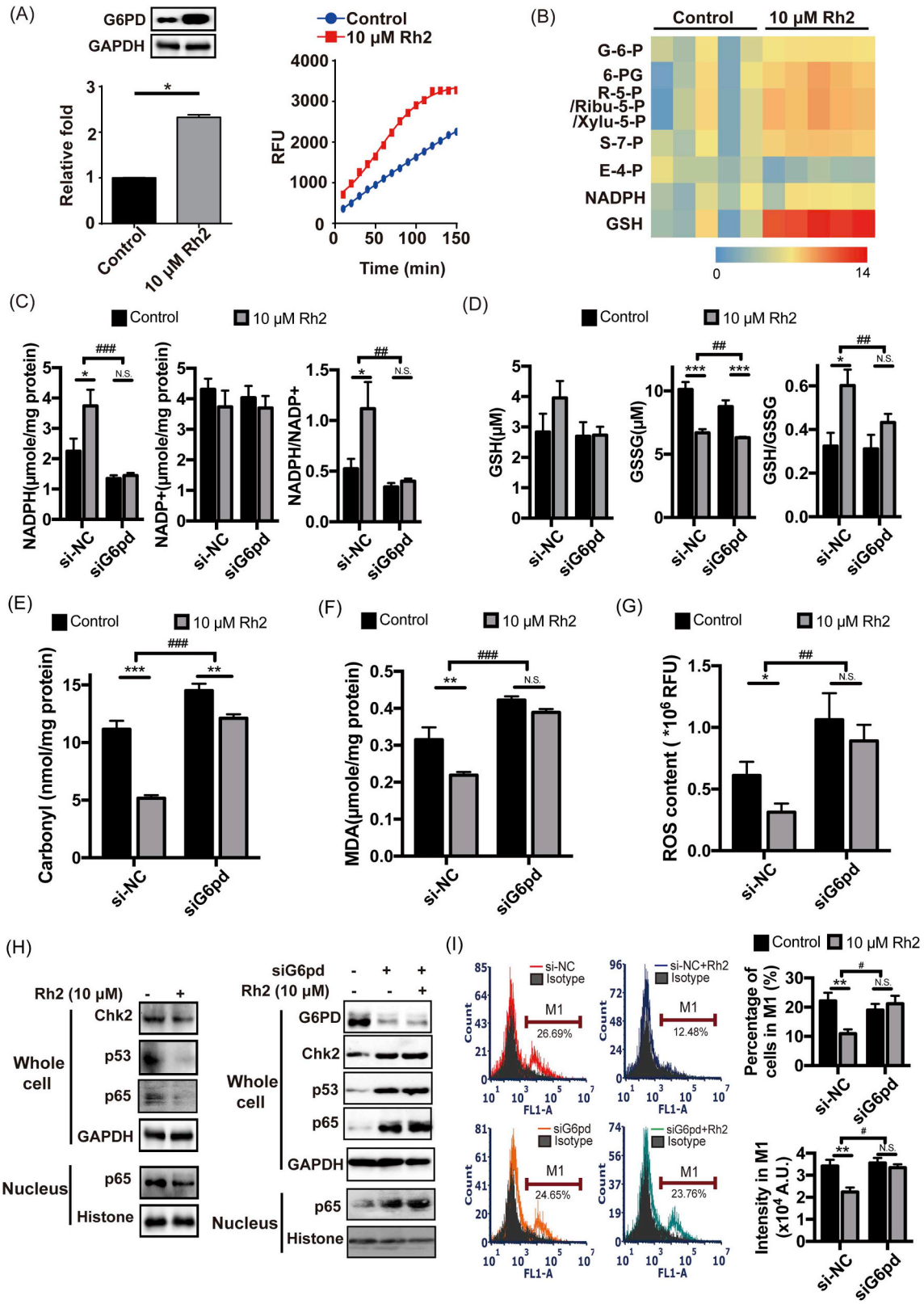

Fig. 2. Rh2 downregulated P-gp by reversing the suppression of PPP. (A) MCF-7 MCTS were treated with Rh2 for 72 h, and the protein and activity levels of G6PD were tested by western blotting and enzyme activity assays, respectively (n = 5). (B) Heatmap of the typical intracellular metabolites in PPP for MCF-7 MCTS in response to Rh2 (n = 5). The effects of Rh2 on the redox status and oxidative damage of MCF-7 MCTS and siG6pd-treated MCF-7 MCTS were analyzed. (C) NADPH and $NADP^+$ levels were tested, and the NADPH/$NADP^+$ ratio was calculated (n = 5). (D) GSH and GSSG levels were tested, and the GSH/GSSG ratio was calculated (n = 5). The levels of intracellular protein carbonylation (E), lipid peroxidation (F) and ROS (G) were tested by commercially available kits (n = 5). (H) The Chk2/p53/p65 pathway was determined by western blot. (I) The protein level of P-gp was determined by flow cytometry (n = 5). All data are presented as the mean ± S.E., *p < 0.05, **p < 0.01, ***p < 0.001. The influence of siG6pd on Rh2 function was further assessed by two-way ANOVA, #p < 0.05, ##p < 0.01, ###p < 0.001.

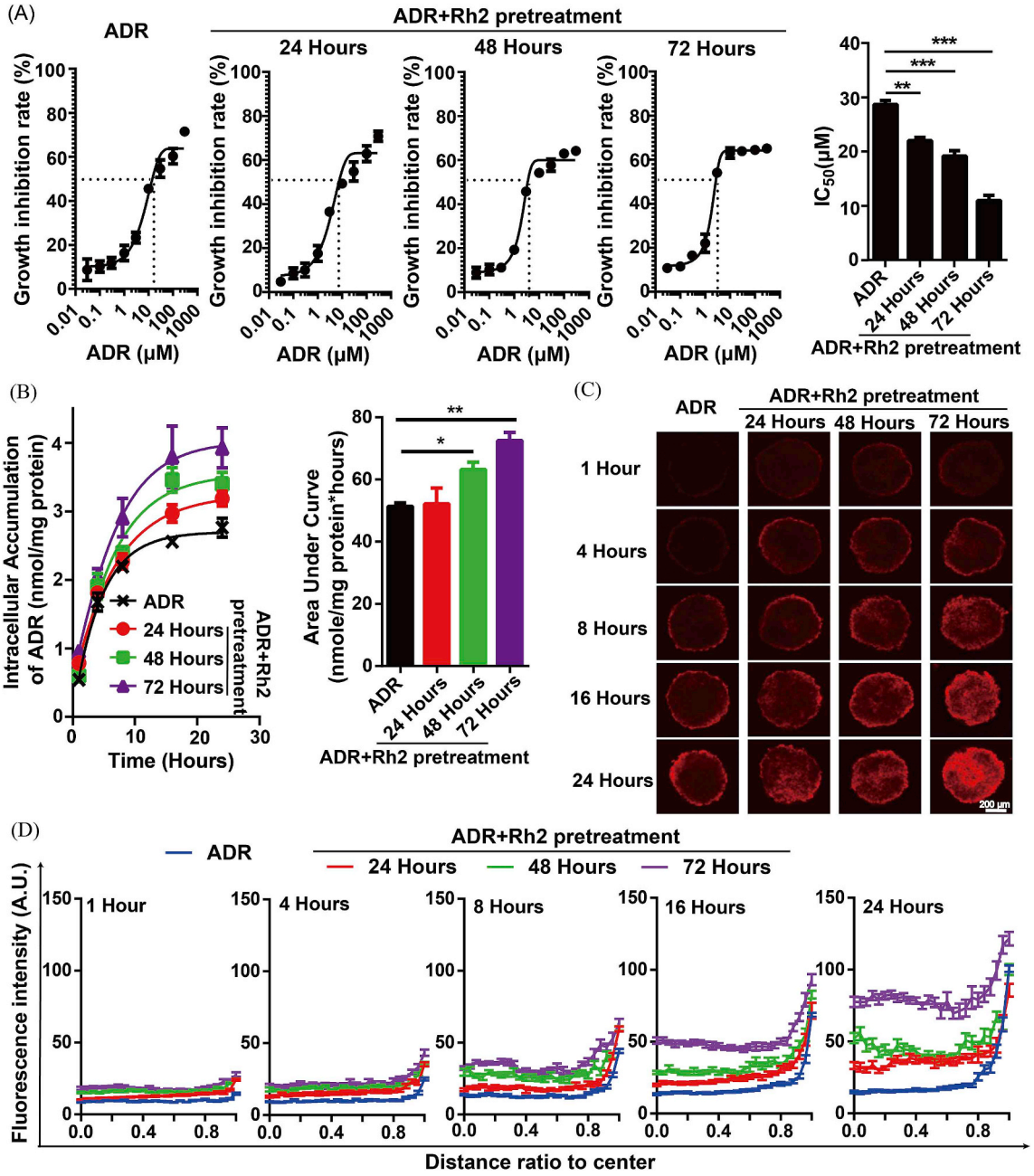

Fig. 3. Rh2 pretreatment and withdrawal enhanced the accumulation of ADR both in the core and peripheral regions. The influence of Rh2 pretreatment and withdrawal on ADR disposition was determined in MCF-7 MCTS. Here, Rh2 pretreatment was administered for different times (24 h, 48 h and 72 h). Following the withdrawal of Rh2, ADR was administered. Then, growth inhibition (A), drug retention (B) and penetration (C) were assayed (n = 5). The fluorescence intensities were plotted (D). Data are presented as the mean ± S.E., *p < 0.05, **p < 0.01, ***p < 0.001.

When MCF-7 MCTS were treated with G6pd siRNA to suppress the activation of PPP by Rh2, the NADPH/$NADP^+$ (Fig. 2C) and GSH/GSSG (Fig. 2D) ratios were no longer increased in the Rh2 treatment group, and no alleviation or extremely weak alleviation of oxidative damage was observed (Fig. 2C-H). Moreover, the downregulation of P-gp by Rh2 in G6pd siRNA-treated MCF-7 MCTS disappeared (Fig. 2I).

3.3. Rh2 pretreatment and withdrawal enhanced the accumulation of ADR both in the core and periphery region

Here, Rh2 pretreatment was administered for different times (24 h, 48 h and 72 h) and then withdrawn, followed by the administration of ADR. As shown in Fig. 3A, the IC_{50} values were decreased by Rh2 pretreatment in a time-dependent manner. The intracellular accumulation of ADR gradually increased with increasing Rh2 pretreatment time (Fig. 3B). Furthermore, the effect of Rh2 pretreatment on the distribution profiles of ADR was assayed. As shown in Fig. 3C and D, Rh2 pretreatment significantly enhanced the ADR fluorescence in both the center and periphery of the MCF-7 MCTS. The enhancement in the center was significantly larger than that in the periphery, and the difference between the fluorescence intensity in the central and peripheral regions became much smaller.

3.4. Coadministration with Rh2 enhanced the accumulation of ADR in the peripheral region

As shown in Fig. 4A, the growth inhibition rate of ADR was significantly increased by Rh2 coadministration for 24 h. In parallel, drug

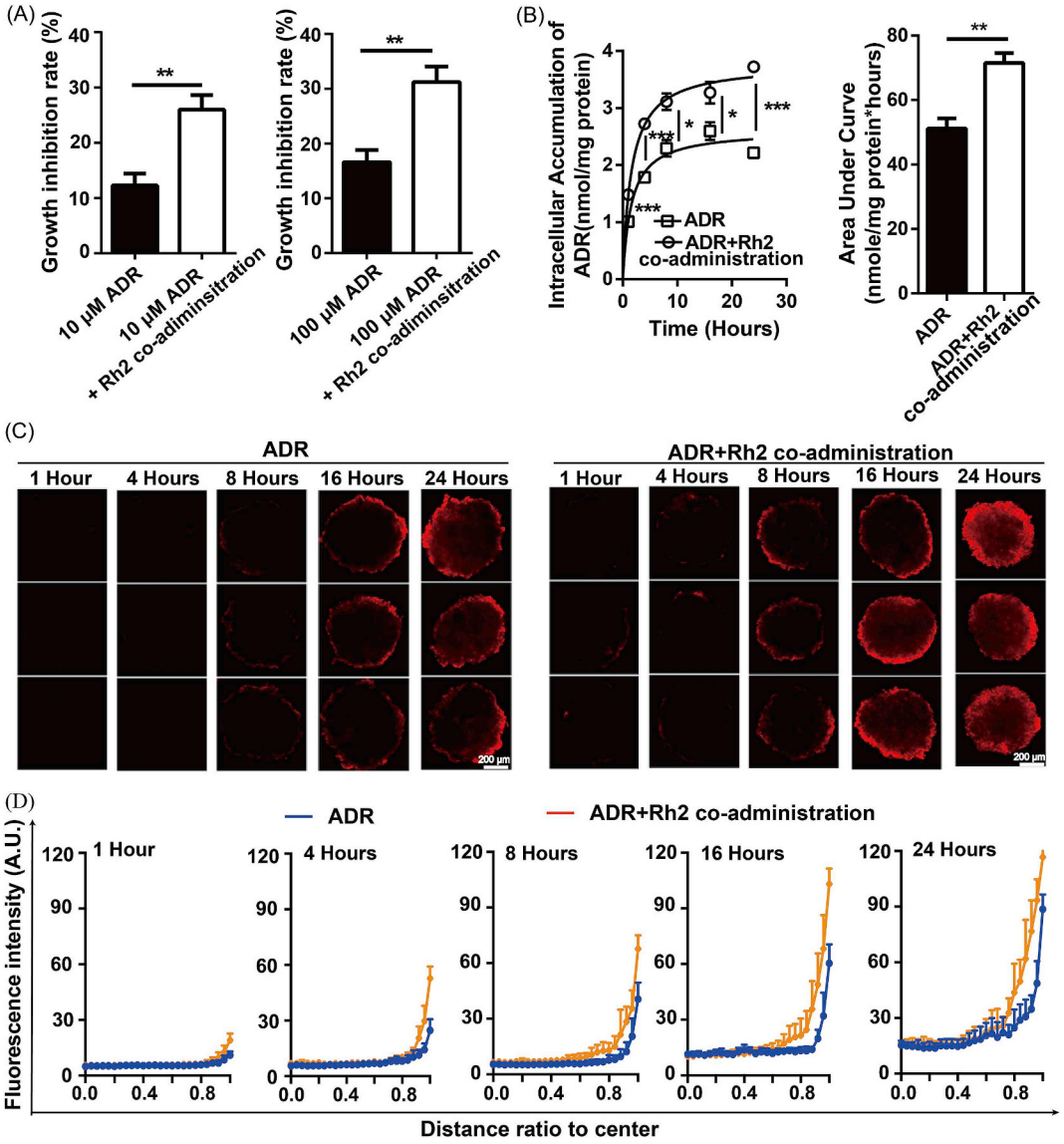

Fig. 4. Coadministration with Rh2 enhanced the accumulation of ADR in the peripheral region. The influence of Rh2 coadministration on ADR disposition was determined in MCF-7 MCTS. After ADR treatment with or without Rh2 coadministration for 24 h, growth inhibition (A), drug retention (B) and penetration (C) were assayed (n = 5). The fluorescence intensities were plotted (D). Data are presented as the mean ± S.E., *p < 0.05, **p < 0.01, ***p < 0.001.

accumulation throughout the MCTS was also increased, and the AUC changed from 51.37 to 71.4 nmol/mg protein*hours (Fig. 4B). Then, the distribution profiles of ADR in MCTS were assayed at different time points after drug administration. After 4 h, the fluorescent signal in the coadministration group became markedly stronger than in the ADR group (Fig. 4C). Plots of the semiquantitative fluorescence intensities against the depth into the MCTS are shown in Fig. 4D. These plots revealed that coadministration with Rh2 enhanced the fluorescence only in the periphery, while no changes were observed in the MCTS core.

3.5. Influence of different Rh2 treatment strategies on the PK-PD profile of ADR at different cell layers

As shown in Fig. 5A, Rh2 coadministration increased the rate and extent of ADR accumulation in peripheral MCTS cells but had little effect on central cells. However, Rh2 pretreatment and withdrawal enhanced ADR accumulation not only on peripheral cells but also on central cells in a time-dependent manner. α and γ were positive in the peripheral cell layers but negative in the central cell layers after Rh2 coadministration. In contrast, α and γ remained positive in all cell layers within the Rh2 pretreatment groups, and larger values of α and γ were observed closer to the center (Fig. 5B). The value of β in the Rh2 coadministration group fluctuated around −0.02 to −0.05 and was much larger than the values of β in the Rh2 pretreatment groups. β decreased in a time-dependent manner after Rh2 pretreatment (Fig. 5B). The intercellular penetration rate was significantly decreased after Rh2 coadministration, as revealed by a 49.8-fold reduction in the ω value. No obvious changes in ω were observed in any of the Rh2 pretreatment groups (Fig. 5B). There were no significant differences in the values of β and ω among the different cell layers in each Rh2 treatment group. The intercellular penetration rates were much smaller than the intracellular retention rates at 1–8 h after Rh2 coadministration, whereas the intercellular penetration rates remained much higher than the intracellular accumulation rates at all the cell layers and all the time points after Rh2 pretreatment (Fig. 5C).

In addition, we explored the relationship between the intracellular retention amount and growth inhibition rates in different drug treatment groups. Growth inhibition rates corresponding to the same ϕ increased with increasing Rh2 pretreatment time (Fig. 5D). Correspondingly, a time-dependent decrease in ψ and increase in r were observed

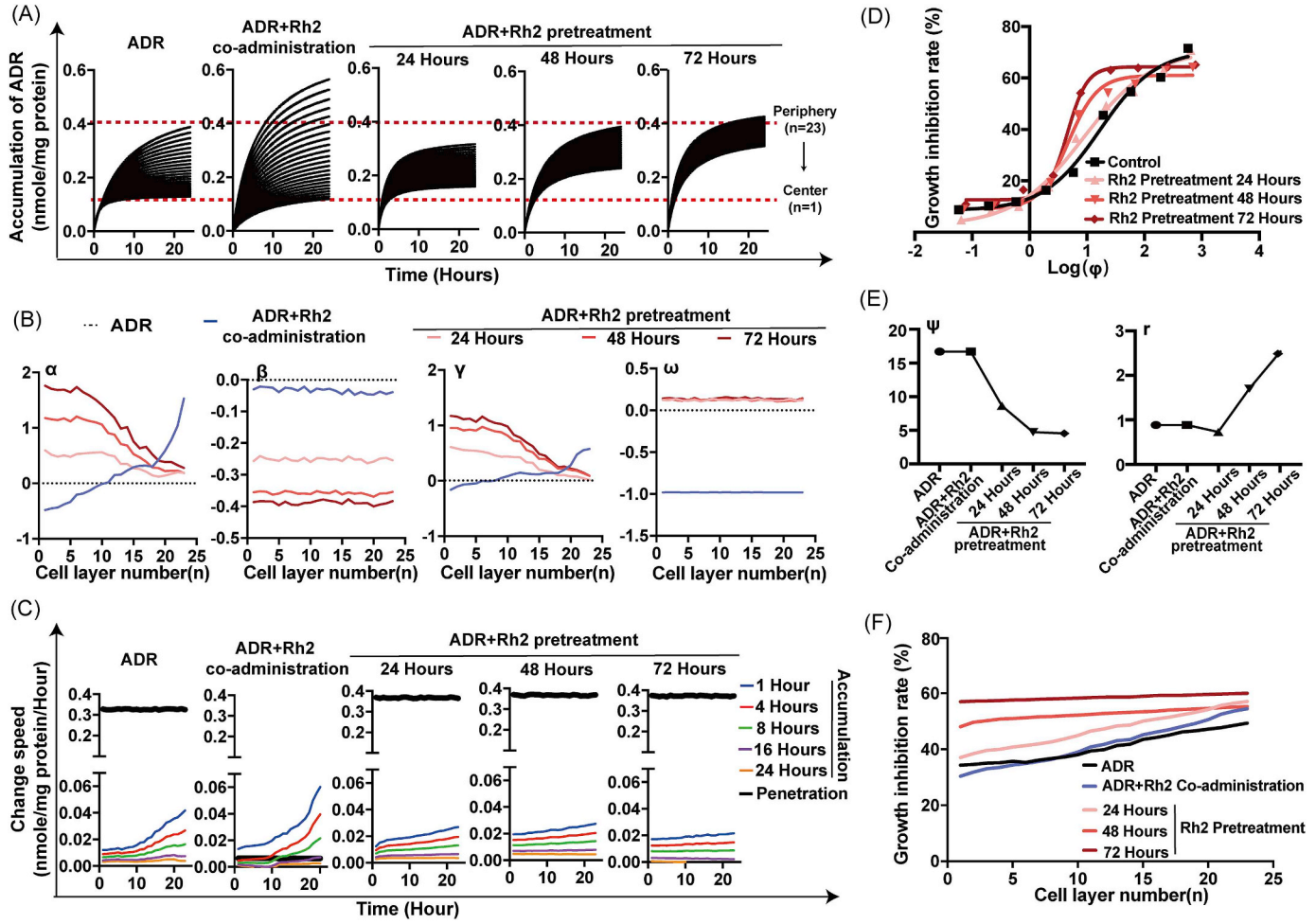

Fig. 5. Influence of different Rh2 treatment strategies on the penetration profile of ADR. (A) ADR accumulations in different cell layers of MCTS are plotted. (B) Kinetic parameters were fitted and are shown. (C) The intercellular diffusion rate and intracellular retention rate were further calculated and are shown. (D) Growth inhibition rates corresponding to the same ϕ increased with increasing Rh2 pretreatment time. (E) PK-PD combined parameters were calculated. (F) The growth inhibition rate for each cell layer after 10 μM ADR treatment for 72 h was predicted.

after Rh2 pretreatment (Fig. 5E). With comprehensive consideration of PK and PD factors, we further calculated the growth inhibition rate for each cell layer after 10 μM ADR treatment for 72 h. As shown in Fig. 5F, the slope of the line for the growth inhibition rate in the Rh2 coadministration group became steeper because of the increases in the peripheral cell layers and decreases in the central cell layers. However, the slopes became quite flat for the Rh2 pretreatment groups. After Rh2 pretreatment for 72 h, the growth inhibition rates with 10 μM ADR at different cell layers were similar.

3.6. Rh2 pretreatment and withdrawal optimized the PK-PD profile of ADR in the tumor mass

Similar to the results observed in vitro, the main metabolites of PPP in tumors significantly increased after Rh2 pretreatment, along with significantly increased protein and activity levels of G6PD (Fig. 6A-C). Importantly, the Chk2/p53/p65 pathway and P-gp expression were also downregulated by Rh2 pretreatment in vivo (Fig. 6C and D). Meanwhile, Rh2 pretreatment enhanced ADR penetration into the tumor mass, as revealed by the significant increase in the fluorescent signal in the center region (Fig. 6E).

Based on the Rh2 pretreatment and withdrawal strategy in vitro, a “ginsenoside Rh2-ADR” sequential regimen was proposed (Fig. 6F). Its antitumor effect was assayed in Balb/c mice implanted with MCF-7 cells. Tumor volumes were measured every day (Fig. 6G). In untreated mice, the tumors rapidly increased in size. However, in mice receiving drug treatments, significantly delayed tumor progression was observed. At the endpoint of drug administration (15 days after treatment), parts of the xenograft tumors in each group were excised and photographed (Fig. 6H). Among the drug treatment groups, the tumor volumes in the ADR treatment group decreased markedly to 0.49-fold of those in the control group. Rh2 single treatment alone did not influence tumor growth, while Rh2 pretreatment moderately decreased tumor volume to 0.76-fold of that in the control group, which was significantly weaker than the effect of ADR. Furthermore, different Rh2/ADR combination treatments showed different influences: Rh2 coadministration with ADR did not markedly enhance the antitumor effects of ADR, while Rh2 pretreatment and withdrawal plus ADR exhibited a significant enhancing effect and showed the greatest antitumor effect, as revealed by the lowest tumor burden (only 0.29-fold that of the control group and 0.62-fold that of the ADR group) (Fig. 6I).

Furthermore, we analyzed tumor regrowth after drug withdrawal and compared the differences in days for drug-treated groups to reach a specified volume (Fig. 6G). At only 7 days after drug withdrawal, the tumor volumes in the “ADR” and “Single-Rh2 + ADR” groups reached the tumor size of the control groups at the endpoint of drug administration, which was half of the time needed in the “Pre-Rh2 + ADR” group. Moreover, the relationship between tumor volume increase and

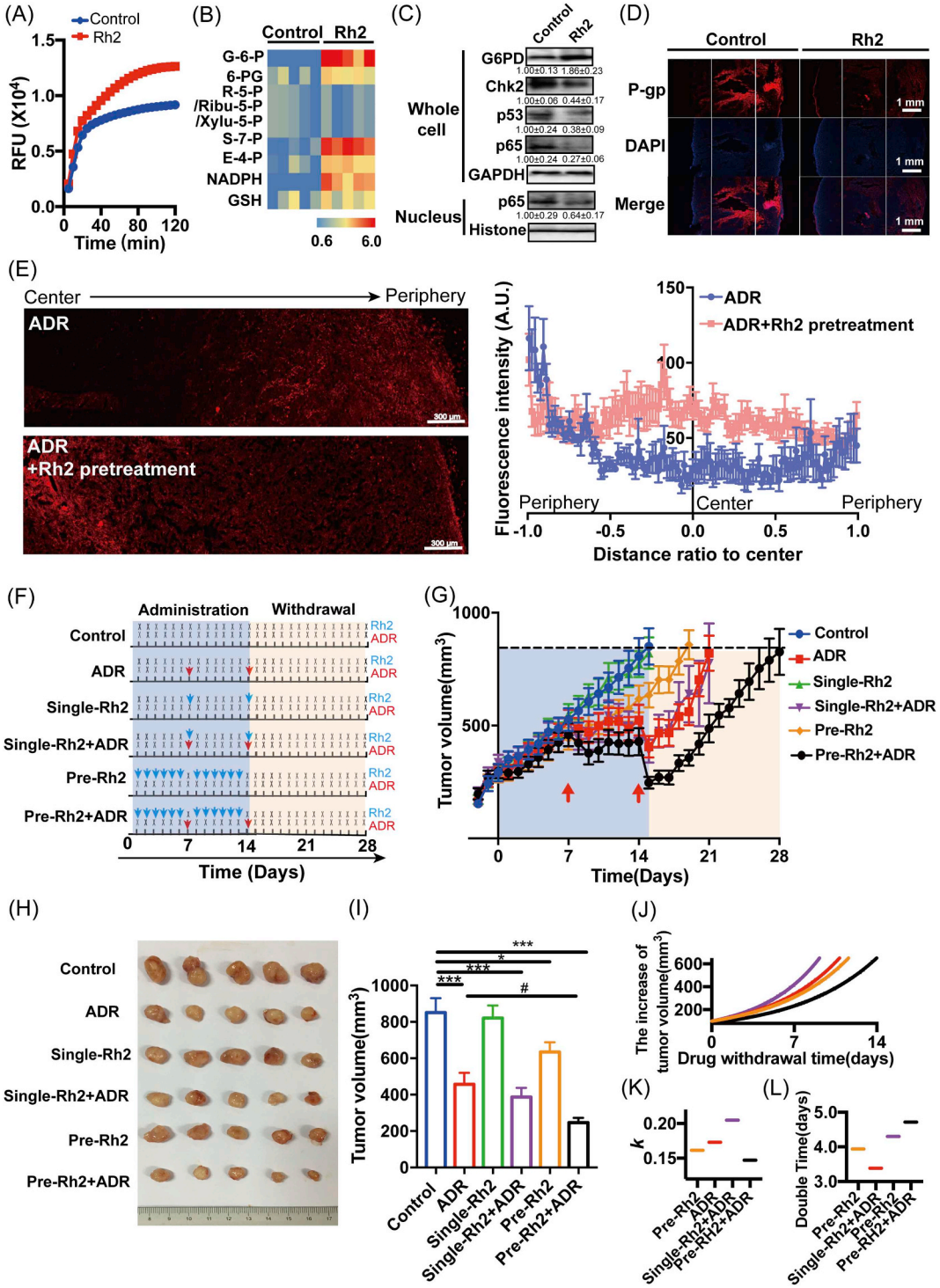

Fig. 6. Influence of different Rh2 treatment strategies on the antitumor effect of ADR. (A) MCF-7-bearing mice were treated with Rh2 for 6 days, and the activity of G6PD in MCF-7 solid tumors was tested by enzyme activity assays (n = 5). (B) Heatmap of the typical intracellular metabolites in PPP for MCF-7 solid tumors in response to Rh2 (n = 5). (C) The G6PD level and the Chk2/p53/p65 pathway were determined by western blot (n = 5). (D) The level of P-gp was tested by immunofluorescence. (E) ADR penetration into the tumor mass with or without Rh2 pretreatment. (F) Schematic presentation of different Rh2 treatment strategies in MCF-7 tumor-bearing mice. (G) Tumor volumes were measured every day, and tumor growth curves were plotted. (H) At the endpoint of drug administration (15 days after treatment), 5 of the mice in each group were sacrificed, and the tumors were dissected and photographed. (I) Tumor volumes at the endpoint in the indicated mice were analyzed and compared. The relationship between the tumor volume increase and drug withdrawal time was simulated (J), and the growth rate constant *k* (K) and doubling time (L) were calculated and compared (n = 7). Data are presented as the mean ± S.E., #p < 0.05, **p < 0.01, ***p < 0.001.

drug withdrawal time was simulated. The tumor regrowth curve in the "Pre-Rh2 + ADR" group was much flatter than those of the other groups (Fig. 6J) with the lowest rate constant *k* (Fig. 6K) and largest doubling time (Fig. 6L).

4. Discussion

Current P-gp inhibitors are designed for strong inhibition of P-gp function. Unfortunately, these inhibitors disrupt the kinetic balance

between intercellular penetration and intracellular accumulation due to excessive increases in intracellular accumulation in cells near vessels, thus resulting in a more inhomogeneous distribution of antitumor drugs and a lack of clinical benefit. Here, we tried to find a novel strategy for the efficient optimization of drug penetration through metabolic reprogramming and redox rebalance-induced P-gp downregulation.

MCT is one of the most commonly used in vitro models for drug delivery assays due to the ability to represent tumor stereostructure and physiological status [15,16]. In contrast to the homogenous drug distribution in the SLC, the fluorescence of ADR in the MCTS was inhomogeneous and decreased from the periphery to the center (Fig. 1F). This was much more similar to the situation in a tumor mass [17]. Furthermore, MCTS also exhibited a similar abnormal metabolic profile and redox imbalance to tumor mass [12]. Thus, we cultured and validated MCF-7 MCTS for screening strategies and evaluating drug penetration (Fig. 1).

20(S)-Ginsenoside Rh2 is a trace active ingredient in red ginseng [18,19]. Due to its extensive but mild effect, Rh2 has been preferentially used as a combination agent in clinical practice rather than a single chemotherapeutic agent. The use of many anticancer agents together with Rh2 has been widely reported, with improved therapeutic effects [17,20,21]. This result was often attributed to the additive effect of the two drugs. Recently, several individual reports revealed that the enhancement effects of Rh2 are based on different mechanisms. Our previous studies found that coadministration with Rh2 increased the effect of ADR on single-layered MCF-7 cells by increasing its intracellular accumulation via P-gp inhibition[13]. Rh2 not only possessed mild noncompetitive P-gp inhibition activity [22] but also repressed ADR-induced P-gp expression through the NF-κB signaling pathway [8,14]. Qian et al. found that Rh2 enhanced the antitumor effect of cyclophosphamide by regulating the intrinsic metabolism [23]. Due to the gap between studies, it is still unknown whether metabolism regulation and P-gp inhibition work separately or in a cascade for the promotion role of Rh2 on chemotherapeutic agents. Nontargeted metabolomics assays indicated that PPP was the predominant pathway influenced when MCTS and tumor mass were treated with Rh2 (Fig. 2A-B and Fig. 6A-B). Previously, we found that PPP was spontaneously impaired along with MCTS and tumor growth. Impaired PPP disturbed redox cycling, and thus Chk2/p53/p65 pathway-mediated P-gp induction [12]. Therefore, we further examined the effect of Rh2 on the above pathway. With PPP reactivation, the redox status rebalanced, as revealed by significant increases in the previously decreased NADPH/$NADP^+$ and GSH/GSSG values and decreases in previously increased oxidative damage and ROS content (Fig. 2C-G). Furthermore, the previous stimulation of the chk2/p53/p65 pathway was inhibited (Fig. 2H), and the high expression of P-gp was downregulated (Fig. 2I). Since several reports had already reported the antioxidative effect of Rh2 [24–26], it was relevant to analyze the contribution of direct antioxidation or PPP activation to the P-gp reversal effect of Rh2. As seen in Fig. 2, the effects of Rh2 on antioxidation and P-gp downregulation in MCF-7 MCTS were significantly weakened by G6PD knockdown, indicating the involvement of PPP in the downregulation of P-gp by Rh2 and a new mechanism for Rh2 antioxidation.

Based on the newly discovered function of Rh2, an Rh2 pretreatment and withdrawal strategy was proposed. Similar to other strategies based on P-gp function interference, Rh2 pretreatment significantly increased average ADR sensitivity and total intracellular accumulation in the whole MCF-7 MCTS. Rh2 pretreatment showed a unique advantage for subsequent drug penetration, which was quite different from other P-gp inhibition strategies: significantly enhanced accumulation of ADR in both the central and peripheral regions of the MCTS (Fig. 3C and D). This phenomenon could not be observed in the Rh2 coadministration group, where Rh2 exhibited a direct P-gp function inhibition effect (Fig. 4). Nevertheless, fluorescence imaging reveals only the penetration depth of drugs and does not provide detailed information on the multiple steps involved in the transport process from tumor vessels to the intended cells. Whether the increased drug accumulation is sufficient to cause an effect remains unclear.

Computational modeling is a cost-effective approach that plays an increasingly important role in quantitatively describing complex kinetic profiles [8,27]. Currently, a wide spectrum of microscopic transport mathematical models have been developed to describe the transport of cancer therapeutics in tumor masses [28]. However, the majority of these models focused on the complex vascular network and provide an estimate of the temporal and spatial fluid flow of intercellular drug penetration[[29,30]]. Only a limited number of studies have focused on the kinetic profiles of intracellular accumulation. Steffen Eikenberry developed a tumor cord model to examine extracellular ADR diffusion and intracellular ADR accumulation [31], and Zhan built a computational model to describe drug transport and uptake in solid tumors [32]. Although these two models innovatively combined intercellular drug diffusion and intracellular drug accumulation, the differences in physiological status and drug disposition profile among cells from different regions were neglected. We previously built an individual-cell-based PK model and successfully described the different intercellular diffusion and intracellular retention kinetics of ADR in each cell layer[9]. Here, we optimized this model with modulation factors and PD model combination. Hence, a novel integrated individual-cell-based integrated PK-PD model was developed. The disposition and efficacy changes of ADR in each cell layer with the Rh2 pretreatment and withdrawal strategy were clarified with quantitative parameters.

In accordance with the observation of fluorescent images, the quantitative retention curves in different cell layers also indicated that Rh2 pretreatment could optimize the homogeneity of ADR distribution: this optimization increased in a time-dependent manner but could not be observed in the Rh2 coadministration group (Fig. 5A). Previously, we found that Rh2 coadministration directly inhibited P-gp efflux function [13]. Here, similar to other P-gp inhibitors [9], Rh2 coadministration resulted in a more inhomogeneous ADR kinetic profile in different cell layers (Fig. 5A), even though it increased total drug accumulation in the whole MCTS (Fig. 4B). Next, we quantitively compared each PK and PD parameter in different Rh2 treatment strategies: Rh2 pretreatment and withdrawal (to interfere with P-gp expression) and Rh2 coadministration (to interfere with P-gp function). Factors α and γ represent the regulatory effects of Rh2 treatment on X_m and P_n, two parameters indicating active transport, respectively. As shown in Fig. 5B, after Rh2 pretreatment and withdrawal, the values of α and γ remained positive in all cell layers. The closer to the core, the larger these two parameters were. Furthermore, the values of α and γ increased with Rh2 pretreatment time (Fig. 5B). The above results indicated that Rh2 pretreatment significantly enhanced X_m and P_n in a pretreatment time-dependent manner and exhibited superior effects in center cells. In the Rh2 coadministration group, the values of α and γ were positive in peripheral cells but negative in central cells, indicating an increase in X_m and P_n in peripheral cells and a decrease in the central cells. Factor ω represents the regulatory effects of Rh2 treatment on K_{pn}, a parameter indicating intercellular drug penetration. K_{pn} remained almost unchanged in the Rh2 pretreatment groups (Fig. 5B), and the intercellular diffusion rates ($\frac{dD_n}{dt}$) remained much higher than the intracellular retention rates ($\frac{dC_n}{dt}$) in all cell layers (Fig. 5C), indicating that no disruption occurred in the kinetic balance. After Rh2 coadministration, the values of ω fluctuated around -0.98 (Fig. 5B), indicating that the values of K_{pn} markedly decreased to only 2% of that in the control group. The intercellular diffusion rates at 1–8 h were much smaller than the drug retention rates in the peripheral cells (Fig. 5C). This meant that in addition to significantly increased intracellular accumulation in peripheral cells, available drug molecules outside the central cells were reciprocally decreased too much to offer sufficient drug supply for central cells, and drug retention in these central cells therefore became slower and lower. Furthermore, Rh2 pretreatment also enhanced drug sensitivity towards ADR in MCTS

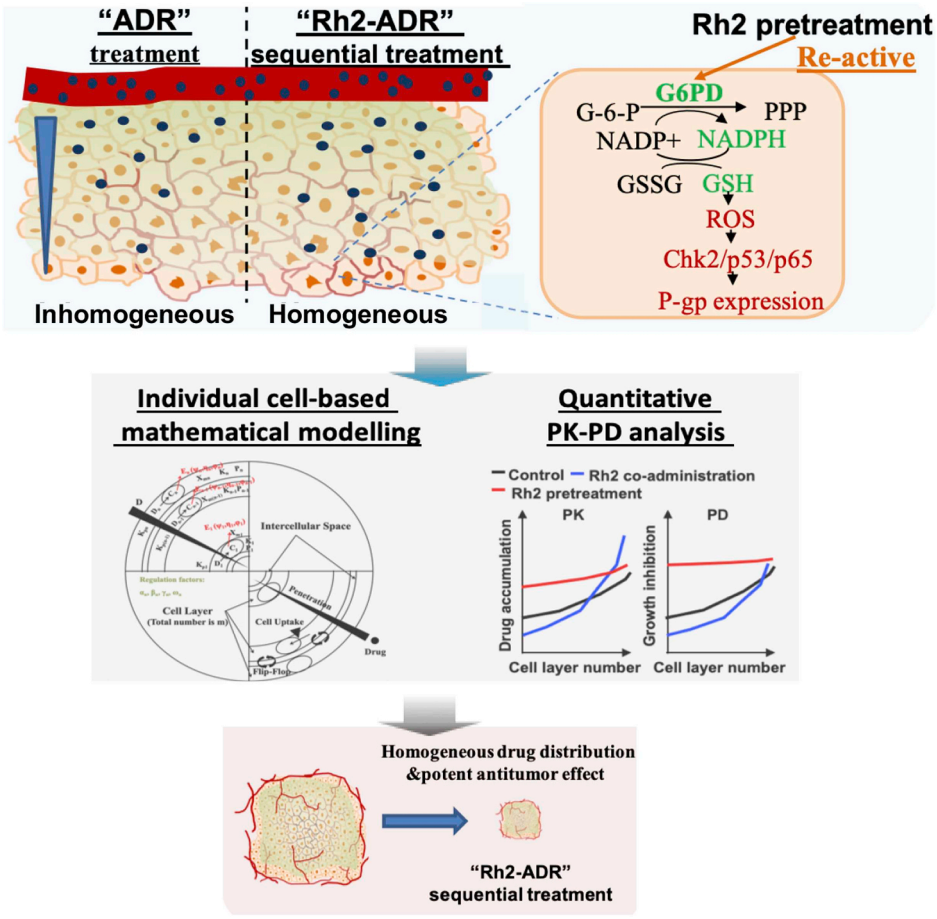

Fig. 7. Scheme of the mathematical model-guided promotion strategy for ADR intratumoral penetration based on metabolic reprogramming and redox rebalancing by ginsenoside Rh2.

(Fig. 5D). Factors ψ and r both represented cell sensitivity to drug administration, and ψ was negatively corrected with drug sensitivity, while r was positively corrected with drug sensitivity. As shown in Fig. 5E, ψ gradually decreased with increasing Rh2 pretreatment time, and r increased. These two parameters remained unchanged in the Rh2 coadministration group. As a comprehensive result of the above changes in PK and PD profiles, the growth inhibition effect of ADR on different cell layers became more homogeneous in the Rh2 pretreatment groups but much more inhomogeneous in the Rh2 coadministration group (Fig. 5F). Specifically, after 72 h of pretreatment with Rh2 prior to ADR administration, no difference in growth inhibition rates could be observed in different cell layers.

Considering the assay based on mathematical modeling and the clinical regimen of ADR, we proposed a "ginsenoside Rh2-ADR" sequential regimen (metabolic reprogramming and redox rebalancing-based P-gp regulation by Rh2), which exhibited a significant enhancing effect. ADR combined with Rh2 pretreatment and withdrawal exhibited the greatest antitumor effect, as revealed by the lowest tumor burden. Furthermore, Rh2 pretreatment and withdrawal also delayed tumor regrowth after drug withdrawal. This enhancement and delay in function could not be observed in the Rh2 coadministration group (simply P-gp function inhibition by Rh2) (Fig. 6).

In summary, we found that Rh2 pretreatment downregulated P-gp expression in MCTS and tumor mass through metabolic reprogramming and redox rebalancing and proposed a "ginsenoside Rh2-ADR" sequential regimen (Rh2 was administered at intervals between two ADR administrations). This regimen had a unique advantage in improving the homogeneity of ADR distribution and exhibited a more potent antitumor effect in vitro and in vivo (Fig. 7).

Author contributions

(1) Study conception and design: Jiali Liu and Jingwei Zhang
(2) Acquisition, analysis and/or interpretation of data: Jiali Liu, Qingyun Cai, Meng Lu, Jianming Liu, Wenjie Wang, Jingwei Zhang
(3) Drafting/revision of the work for intellectual content and context: Jiali Liu, Qingyun Cai, Fang Zhou, Minjie Sun and Guangji Wang
(4) Final approval and overall responsibility for the published work: Jiali Liu, Qingyun Cai and Jingwei Zhang

All authors reviewed the manuscript.

Research data for this article

All code generated or analyzed during this study and the original data for figures in the paper are available from the corresponding author upon request.

Declaration of competing interest

The authors declare no conflicts of interest.

Acknowledgments

The authors sincerely thank the postgraduates in the Key Laboratory of Drug Metabolism and Pharmacokinetics (China Pharmaceutical University, Nanjing, China) for their kind assistance.

This work was supported by the China National Nature Science Foundation [No. 81803625, 81703600, 81773989]; China Postdoctoral

Science Found [No. 2018M642374]; the Jiangsu postdoctoral grant program [No. 2018Z061]; the Jiangsu Province Nature Science Foundation [No. BK20180558]; six talent peaks project in Jiangsu Province (YY-060); the Major State Basic Research Development Program of China [2017YFA0205400]; National Research Council of Science and Technology Major Project of China (2017ZX09201004-019, 2019ZX09721001-006-005, 2019ZX09302023); Leading technology foundation research project of Jiangsu Province(BK20192005); "Double First-Class" University project (CPU2018GF01, China).

Appendix A. Supplementary data

Supplementary data to this article can be found online at https://doi.org/10.1016/j.redox.2020.101452.

References

[1] M.W. Dewhirst, T.W. Secomb, Transport of drugs from blood vessels to tumour tissue, Nat. Rev. Canc. 17 (2017) 738–750.
[2] R.K. Jain, Normalizing tumor microenvironment to treat cancer: bench to bedside to biomarkers, J. Clin. Oncol. 31 (2013) 2205–2218 official journal of the American Society of Clinical Oncology.
[3] A.M. Al-Abd, Z.K. Aljehani, R.W. Gazzaz, S.H. Fakhri, A.H. Jabbad, A.M. Alahdal, V.P. Torchilin, Pharmacokinetic strategies to improve drug penetration and entrapment within solid tumors, J. Contr. Release 219 (2015) 269–277.
[4] H.M. Abdallah, A.M. Al-Abd, R.S. El-Dine, A.M. El-Halawany, P-glycoprotein inhibitors of natural origin as potential tumor chemo-sensitizers: a review, J. Adv. Res. 6 (2015) 45–62.
[5] B. Goldman, Multidrug resistance: can new drugs help chemotherapy score against cancer? J. Natl. Cancer Inst. 95 (2003) 255–257.
[6] L.D. Cripe, H. Uno, E.M. Paietta, M.R. Litzow, R.P. Ketterling, J.M. Bennett, J.M. Rowe, H.M. Lazarus, S. Luger, M.S. Tallman, Zosuquidar, a novel modulator of P-glycoprotein, does not improve the outcome of older patients with newly diagnosed acute myeloid leukemia: a randomized, placebo-controlled trial of the Eastern Cooperative Oncology Group 3999, Blood 116 (2010) 4077–4085.
[7] A.R. Kirtane, S.M. Kalscheuer, J. Panyam, Exploiting nanotechnology to overcome tumor drug resistance: challenges and opportunities, Adv. Drug Deliv. Rev. 65 (2013) 1731–1747.
[8] M. Lu, F. Zhou, K. Hao, J. Liu, Q. Chen, P. Ni, H. Zhou, G. Wang, J. Zhang, Alternation of adriamycin penetration kinetics in MCF-7 cells from 2D to 3D culture based on P-gp expression through the Chk2/p53/NF-kappaB pathway, Biochem. Pharmacol. 93 (2015) 210–220.
[9] J. Liu, F. Yan, H. Chen, W. Wang, W. Liu, K. Hao, G. Wang, F. Zhou, J. Zhang, A novel individual-cell-based mathematical model based on multicellular tumour spheroids for evaluating doxorubicin-related delivery in avascular regions, Br. J. Pharmacol. 174 (2017) 2862–2879.
[10] P. Joshi, R.A. Vishwakarma, S.B. Bharate, Natural alkaloids as P-gp inhibitors for multidrug resistance reversal in cancer, Eur. J. Med. Chem. 138 (2017) 273–292.
[11] J.K. Tunggal, T. Melo, J.R. Ballinger, I.F. Tannock, The influence of expression of P-glycoprotein on the penetration of anticancer drugs through multicellular layers, Int. J. Canc. 86 (2000) 101–107.
[12] W. Wang, Q. Cai, F. Zhou, J. Liu, X. Jin, P. Ni, M. Lu, G. Wang, J. Zhang, Impaired pentose phosphate pathway in the development of 3D MCF-7 cells mediated intracellular redox disturbance and multi-cellular resistance without drug induction, Redox Biol. 15 (2018) 253–265.
[13] J. Zhang, F. Zhou, X. Wu, X. Zhang, Y. Chen, B.S. Zha, F. Niu, M. Lu, G. Hao, Y. Sun, J. Sun, Y. Peng, G. Wang, Cellular pharmacokinetic mechanisms of adriamycin resistance and its modulation by 20(S)-ginsenoside Rh2 in MCF-7/Adr cells, Br. J. Pharmacol. 165 (2012) 120–134.
[14] J. Zhang, M. Lu, F. Zhou, H. Sun, G. Hao, X. Wu, G. Wang, Key role of nuclear factor-kappaB in the cellular pharmacokinetics of adriamycin in MCF-7/Adr cells: the potential mechanism for synergy with 20(S)-ginsenoside Rh2, Drug Metab. Dispos. 40 (2012) 1900–1908.
[15] S.M. Ong, Z. Zhao, T. Arooz, D. Zhao, S. Zhang, T. Du, M. Wasser, D. van Noort, H. Yu, Engineering a scaffold-free 3D tumor model for in vitro drug penetration studies, Biomaterials 31 (2010) 1180–1190.
[16] K.K. Winner, M.P. Steinkamp, R.J. Lee, M. Swat, C.Y. Muller, M.E. Moses, Y. Jiang, B.S. Wilson, Spatial modeling of drug delivery routes for treatment of disseminated ovarian cancer, Canc. Res 76 (2016) 1320–1334.
[17] B.W. Huang, J.Q. Gao, Application of 3D cultured multicellular spheroid tumor models in tumor-targeted drug delivery system research, J. Contr. Release 270 (2018) 246–259.
[18] J.H. Kim, M. Kim, S.M. Yun, S. Lee, J.H. No, D.H. Suh, K. Kim, Y.B. Kim, Ginsenoside Rh2 induces apoptosis and inhibits epithelial-mesenchymal transition in HEC1A and Ishikawa endometrial cancer cells, Biomed. Pharmacother. 96 (2017) 871–876.
[19] Q. Gao, J. Zheng, Ginsenoside Rh2 inhibits prostate cancer cell growth through suppression of microRNA-4295 that activates CDKN1A, Cell Prolif 51 (2018) e12438.
[20] W. Chen, Y. Qiu, Ginsenoside Rh2 targets EGFR by up-regulation of miR-491 to enhance anti-tumor activity in hepatitis B virus-related hepatocellular carcinoma, Cell Biochem. Biophys. 72 (2015) 325–331.
[21] D.L. Lv, L. Chen, W. Ding, W. Zhang, H.L. Wang, S. Wang, W.B. Liu, Ginsenoside G-Rh2 synergizes with SMI-4a in anti-melanoma activity through autophagic cell death, Chin. Med. 13 (2018) 11.
[22] J. Zhang, F. Zhou, X. Wu, Y. Gu, H. Ai, Y. Zheng, Y. Li, X. Zhang, G. Hao, J. Sun, Y. Peng, G. Wang, 20(S)-ginsenoside Rh2 noncompetitively inhibits P-glycoprotein in vitro and in vivo: a case for herb-drug interactions, Drug Metab. Dispos. 38 (2010) 2179–2187.
[23] Y. Qian, R. Huang, S. Li, R. Xie, B. Qian, Z. Zhang, L. Li, B. Wang, C. Tian, J. Yang, M. Xiang, Ginsenoside Rh2 reverses cyclophosphamide-induced immune deficiency by regulating fatty acid metabolism, J. Leukoc. Biol. 106 (2019) 1089–1100.
[24] W.Y. Choi, H.W. Lim, C.J. Lim, Anti-inflammatory, antioxidative and matrix metalloproteinase inhibitory properties of 20(R)-ginsenoside Rh2 in cultured macrophages and keratinocytes, J. Pharm. Pharmacol. 65 (2013) 310–316.
[25] L. Bai, J. Gao, F. Wei, J. Zhao, D. Wang, J. Wei, Therapeutic potential of ginsenosides as an adjuvant treatment for diabetes, Front. Pharmacol. 9 (2018) 423.
[26] Z. Cheng, M. Zhang, C. Ling, Y. Zhu, H. Ren, C. Hong, J. Qin, T. Liu, J. Wang, Neuroprotective effects of ginsenosides against cerebral ischemia, Molecules (2019) 24.
[27] K.O. Hicks, F.B. Pruijn, J.R. Sturman, W.A. Denny, W.R. Wilson, Multicellular resistance to tirapazamine is due to restricted extravascular transport: a pharmacokinetic/pharmacodynamic study in HT29 multicellular layer cultures, Canc. Res 63 (2003) 5970–5977.
[28] W. Zhan, M. Alamer, X.Y. Xu, Computational modelling of drug delivery to solid tumour: understanding the interplay between chemotherapeutics and biological system for optimised delivery systems, Adv. Drug Deliv. Rev. 132 (2018) 81–103.
[29] E. Kim, S. Stamatelos, J. Cebulla, Z.M. Bhujwalla, A.S. Popel, A.P. Pathak, Multiscale imaging and computational modeling of blood flow in the tumor vasculature, Ann. Biomed. Eng. 40 (2012) 2425–2441.
[30] S.K. Stamatelos, E. Kim, A.P. Pathak, A.S. Popel, A bioimage informatics based reconstruction of breast tumor microvasculature with computational blood flow predictions, Microvasc. Res. 91 (2014) 8–21.
[31] S. Eikenberry, A tumor cord model for doxorubicin delivery and dose optimization in solid tumors, Theor. Biol. Med. Model. 6 (2009) 16.
[32] W. Zhan, W. Gedroyc, X.Y. Xu, Mathematical modelling of drug transport and uptake in a realistic model of solid tumour, Protein Pept. Lett. 21 (2014) 1146–1156.